Free flow wind speed from a blade-mounted flow sensor

Mads Mølgaard Pedersen[1], Torben Juul Larsen[1], Helge Aagaard Madsen[1], and Søren Juhl Andersen[2]

[1]Wind Energy Department, Technical University of Denmark, Frederiksborgvej 399, 4000 Roskilde, Denmark
[2]Wind Energy Department, Technical University of Denmark, Nils Koppels Alle, Building 403, 2800 Kgs. Lyngby, Denmark

Correspondence to: Mads M. Pedersen (mmpe@dtu.dk)

Abstract. This paper presents a method for obtaining the free inflow velocities from a 3D flow sensor mounted on the blade of a wind turbine.

From its position on the rotating blade, e.g. one third from the tip, a blade mounted flow sensor (BMFS) is able to provide valuable information about the turbulent sheared inflow in different regions of the rotor. At the rotor, however, the inflow is affected by the wind turbine, and in most cases the wind of interest is the inflow that the wind turbine is exposed to; i.e. the free inflow velocities.

The current method applies a combination of aerodynamic models and procedures to estimate the induced velocities, i.e. the disturbance of the flow field caused by the wind turbine. These velocities are subtracted from the flow velocities measured by the BMFS to obtain the free inflow velocities. Aeroelastic codes, like HAWC2, typically use a similar approach to calculate the induction, but they use it for the reversed process, i.e. they add the induction to the free inflow to get the flow velocities at the blades which are required to calculate the resulting aerodynamic forces.

The aerodynamic models included in the current method comprise blade-element-momentum (BEM) based models for axial and tangential induction, a radial induction model and tip loss correction as well as models for skew and dynamic inflow.

It is shown that the method is able to calculate the free inflow velocities with high accuracy when applied to aeroelastic HAWC2 simulations with a stiff structural model while some deviations are seen in simulations with a flexible structure.

Furthermore, the method is tested on simulations performed by a flexible structural model coupled with a large eddy simulation (LES) flow solver. The results of this higher fidelity verification confirm the HAWC2-based conclusion.

1 List of symbols

a	Axial induction factor
a'	Tangential induction factor
a_r	Radial induction factor
c	Chord length
C_T	Trust coefficient
$C_{T,avg}$	Average trust coefficient
C_x	Lift and drag coefficient projected into x^R
C_y	Lift and drag coefficient projected into y^R
D	Aerodynamic drag force
F_a	Thrust reduction factor in skew inflow model
F_{azi}	Azimuthal dependent reduction factor in skew inflow model
F_{tip}	Prandtl's tip loss factor
f_W	Function calculating induced velocities
$k_i, i = 0..3$	Constants
k_x, k_y	Factors in skew inflow model
L	Aerodynamic lift force
$\mathrm{LP}(\tau, X)$	Low pass filter with filter characteristics, τ
N_B	Number of blades
r	Sensor radius
R	Blade tip radius
$\boldsymbol{T_{ab}}$	Transformation matrix from coordinate system a to coordinate system b
$\boldsymbol{V_r}$	Measured flow velocity at rotor plane
$\boldsymbol{V_{rel}}$	Measured velocity relative to the sensor
V_{relxy}	Relative wind speed in the (x^R, y^R)-plane
$\boldsymbol{V_{rot}}$	Velocity of sensor due to rotor rotation
$\boldsymbol{V_s}$	Velocity of the sensor
$\boldsymbol{V_0}$	Free flow wind speed
$\boldsymbol{V_{0,est}}$	Estimated free flow wind speed
$\boldsymbol{W}$	Induced velocity
$\boldsymbol{W_{est}}$	Estimated induced velocity
$\boldsymbol{W_{avg}}$	Average induced velocity
$\boldsymbol{W_{dyn}}$	Induced velocity, estimated using dynamic inflow model
$\boldsymbol{W_{dyn,azi}}$	Induced velocity, estimated using dynamic inflow model applied to fixed azimuthal positions

α	Angle of attack
χ	Angle between $\boldsymbol{V_r}$ and rotor plane
χ_{hor}	Horizontal angle between $\boldsymbol{V_r}$ and rotor plane
χ_{ver}	Vertical angle between $\boldsymbol{V_r}$ and rotor plane
ω	Angular rotor velocity
ϕ	Angle between rotor plane and V_{relxy}
Φ_r	Angle between rotor plane and $\boldsymbol{V_0}$
θ_{pitch}	Pitch angle
θ_{rotor}	Rotor azimuthal position
θ_{tt}	Tower top deflection angle
θ_{twist}	Twist angle

Coordinate systems, see section 3.1

G	Ground coordinate system
R	Rotating rotor coordinate system
S	Blade section coordinate system

Modifiers

*	Actual velocity or deflected direction (opposed to the assumed velocity or undeflected direction)

2 Introduction

5 Detailed knowledge about the atmospheric turbulent wind and its variation is essential for understanding and analysing many
aspects regarding wind turbines, e.g. load conditions, power generation, noise aspects, and fatigue and extreme loads (Elliott
and Cadogan, 1990; Larsen et al., 2005; Barlas et al., 2012; Madsen, 2014; St. Martin et al., 2016)

The wind of interest is the free undisturbed turbulent inflow, but at the location of the wind turbine rotor. The problem is
that this free wind is immeasurable, as the inflow is influenced by the presence of the rotor itself: near the turbine, the flow is
10 disturbed by the turbine, and further away, the wind is different. The ideal measure, therefore, is the free flow wind speed at
the position of the turbine, i.e. the wind speed as it would have been at the same location and time without the turbine.

A cup or sonic anemometer at a nearby met mast, e.g., 2-3 diameters away, measures the free flow wind when not in the
wake of the turbine or the mast, but smaller turbulence structures will be different due to the distance. As these structures have
only limited influence on e.g. 10 min statistics, the wind speeds measured by met masts are still valuable and extensively used.
15 The wind speed measured by a nacelle- or spinner-mounted anemometer is influenced by the turbine. This influence is
measurable more than one diameter upstream (Meyer Forsting et al., 2017) and continues until the wake is recovered far
downstream. This means that a model or calibration function is required to estimate the free flow wind speed from a nacelle-
or spinner-mounted anemometer.

The turbine is, however, not only exposed to the wind at the hub centre, and with the long blades of modern wind turbines, the wind-speed variations within the rotor may be considerable. This variation can be measured using lidars which are typically ground or nacelle based. From the nacelle, a lidar is able to measure the inflow field some distance upstream while the inflow field at the rotor plane can be measured using a set of ground-based scanning lidars (Mikkelsen et al., 2008, 2010; Scholbrock

5   et al., 2015; Wagner et al., 2015). Nevertheless, the problem is the same; the lidars must either measure outside the induction zone to measure the free inflow or use a model to compensate for the presence of the turbine. Troldborg and Meyer Forsting (2017) describe a simple analytical model that is able to estimate the free wind speed, appropriate for power curves, from lidar measurements. The model is applicable for any rotor down to one rotor radius upstream.

Another option is to mount a flow sensor directly on the blade, e.g. one third from the tip. From this location, the sensor

10   sweeps the rotor area and is thereby able to measure a lot of the variation that takes place within the rotor area.

Blade-mounted five-hole pitot tubes have been used in several research projects (Madsen, 1991; Brand et al., 1996; Petersen and Aagaard Madsen, 1997; Simms et al., 1999; Schepers et al., 2002; Madsen et al., 2003, 2010b; Medina et al., 2011), but other types of sensors could be used as well. In the current context, a blade-mounted flow sensor (BMFS) is assumed to measure the 3D inflow velocity at its position, i.e. the temporal resolution of a point fixed in space is limited to once per revolution,

15   and multiple sensors are required for measuring in both the inner and outer part of the rotor. From the 3D inflow velocities measured by a BMFS, information about the angle of attack, relative velocity and the instant wind speed at the rotor plane can be extracted. This information can be used as input for the control of individual pitch or active trailing edge flaps to optimise power and reduce loads and noise (Larsen et al., 2005; Barlas et al., 2012; Kragh and Hansen, 2012; Kragh et al., 2012; Madsen, 2014). Another application is the generation of relative power or load curves that can be compared between similar

20   periods or turbines. These relative curves can be used to investigate e.g. aerodynamic modifications or detect performance issues (Pedersen et al., 2017).

As a BMFS is inside the induction zone, a model is required to estimate the free flow wind speed. In this case, however, well-defined models already exist as they are used in aeroelastic codes, e.g. HAWC2, to simulate the flow that generates the aerodynamic forces at the blades (Larsen and Hansen, 2007; Madsen et al., 2018). These models calculate the disturbance of

25   the flow caused by the turbine in terms of the induced velocities, which are then added to the free flow velocity to get the disturbed wind speed at the blades. Reversing this process, the free flow wind speed can be obtained by subtracting the induced velocities from the measured velocities.

This paper describes the necessary aerodynamic models as well as a procedure to obtain the free flow wind speed from a BMFS. A preliminary implementation of the method has previously been applied to measurements of a full-scale wind turbine

30   with a blade-mounted five-hole pitot tube to estimate the free inflow in different wake conditions (Pedersen et al., 2015).

To test the method, both the disturbed and the immeasurable free flow wind speeds are required. A real validation against measurements is therefore infeasible. Instead, the method is tested in two independent simulated environments.

The first environment is simulated by HAWC2, a nonlinear aeroelastic code intended for computing wind turbine response in the time domain (Larsen and Hansen, 2007). HAWC2 uses Taylor's well-known frozen turbulence hypothesis (Taylor, 1938)

35   and a combination of aerodynamic models, which are similar to the models of the current method, to calculate the disturbed

flow velocity at the rotor plane. Both the free inflow and the disturbed flow at the rotor plane are therefore directly available for verification of the method.

In the second environment, the simulations are performed by the structural model of FLEX5 (Øye, 1996) coupled with the large eddy simulation (LES) flow solver, EllipSys3D (Michelsen, 1992; Sørensen, 1995). This environment is completely

5 independent of the aerodynamic models of the current method as well as Taylor's frozen turbulence hypothesis and is therefore valuable as a high fidelity verification. In this case, the free undisturbed inflow is obtained from a separate equivalent simulation where the effects of the aerodynamic forces on the flow are disabled.

3 Method

This section presents the aerodynamic models and the procedure used to obtain the free inflow velocities from a BMFS.

10 ### 3.1 Coordinate systems

The coordinate systems used in this paper are listed in table 1.

Table 1. Coordinate systems used in this paper

Coordinate system	Abbreviation	Definition
Blade section coordinates	S	x^S: Along chord line from centre towards leading edge
		y^S: Perpendicular to chord line centre to suction side
		z^S: Aligned blade center line from root to tip
Rotating rotor coordinates	R	x^R: Tangential in rotational direction
		y^R: Aligned with main shaft in direction of the wind
		z^R: Aligned with the blade on which the BMFS is mounted
Ground coordinates	G	x^G: Horizontal left, perpendicular to the main shaft when seen from the front
		y^G: Horizontal in direction of main shaft
		z^G: Vertical, down

Transformation matrices are used to map velocities between the coordinate systems. As an example, the transformation matrix, $\boldsymbol{T_{RG}}$, describes the rotating-rotor coordinate-system axes in ground coordinates. $\boldsymbol{T_{RG}}$ can be used to map velocities in rotor coordinates, $\boldsymbol{V^R}$, to velocities in ground coordinates, $\boldsymbol{V^G}$:

15 $$\boldsymbol{V^G} = \boldsymbol{T_{RG}} \boldsymbol{V^R} \tag{1}$$

3.2 Wind speed from a BMFS

The method described in this paper take as input the effective 3D inflow velocities measured relative to the blade, locally at the rotor plane, i.e. including the effects caused by the presence of the turbine.

Near the airfoil, the local flow field is deflected and the speed is also influenced by the bound circulation on the surface of

5 the airfoil; see the example in Fig. 1. As seen, this effect has a huge impact on the flow velocity measured near the airfoil and must therefore be compensated for before applying the current method. In the current study, however, it is neglected as the two verification environments, HAWC2 and EllipSys3D/Flex5, do not model the surface of the airfoils.

Shen et al. (2006, 2009), Guntur and Sørensen (2014) and Rahimi et al. (2017) present several methods to calculate the flow near the airfoil that also take 3D effects into account, but the methods require information that cannot be obtained directly from

10 a BMFS. Pedersen et al. (2017) describes how to obtain the effective 3D inflow from the relative wind speed and two perpendicular angles measured by a blade-mounted five-hole pitot, including compensation for bound circulation. The compensation method uses a look-up table generated by 2D computational fluid dynamic (CFD) simulations, thus neglecting 3D effects, and tip- and root vortices.
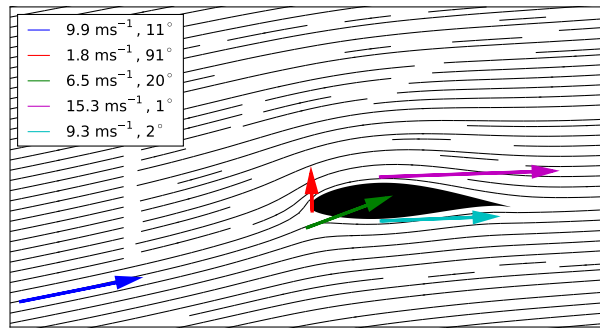
Figure 1. Near the airfoil, the flow is disturbed by upwash and stagnation. This effect is not included in the current method

From the relative velocity, V_{rel}, the wind speed at the rotor plane, V_r, is found by subtracting the velocity of the sensor, V_s:

$$V_r = V_{rel} - V_s \tag{2}$$

In this study, the sensor velocity, V_s, includes movement due to rotor rotation and pitch motion. Structural dynamics, e.g. blade deflection, will therefore result in a mismatch between the assumed and the actual sensor velocity.

3.3 Aerodynamic models

20 The wind speed measured in the rotor plane of an operating wind turbine is different from the free flow wind speed that would have been present at the same time and location if the wind turbine was absent. The difference is induced by the wind turbine
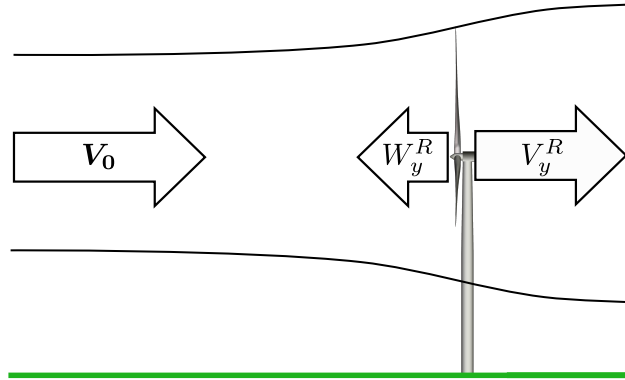
Figure 2. At the rotor plane, the free inflow wind velocity, $\boldsymbol{V_0}$, is reduced by the axial induction, W_y^R. A sensor at the rotor plan will therefore measure the reduced velocity, $V_{r,y}^R$, in the axial direction

induction and is rather complex. In this section, a set of simplified engineering aerodynamic models that each explains elements of the induction are presented. One can argue that the models are too simple compared to the physical processes. In general, however, the loads simulated by aeroelastic codes that use these models are found to agree well with measured loads; see e.g. Larsen et al. (2013). The models are therefore expected to be appropriate for the reverse process too.

5   The aerodynamic models in aeroelastic codes like FAST, Flex5, Bladed and HAWC2 is based on the Blade Element Momentum (BEM) model first presented by Glauert (1935). The original formulation, however, was derived for one-dimensional, steady and uniform inflow, which is far from the conditions that a real turbine operates in. The BEM model is therefore typically modified and combined with additional sub models, e.g. for tip loss and for skew and dynamic inflow. In this study, the aerodynamic model is based on the HAWC2 implementation (Madsen et al., 2018).

10 **3.3.1   Axial induction**

When operating, a wind turbine extracts kinetic energy from the wind by reducing the axial wind speed. This reduction is called the axial induction, W_y^R; see Fig. 2.

The axial induced wind speed is defined in terms of the axial induction factor, a:

$$W_y^R = a|\boldsymbol{V_0}| \tag{3}$$

15 where $\boldsymbol{V_0}$ is the free inflow velocity.

For laminar flow through the rotor, the axial induction factor is related to the thrust coefficient, C_T, by

$$C_T = 4a(1-a) \tag{4}$$
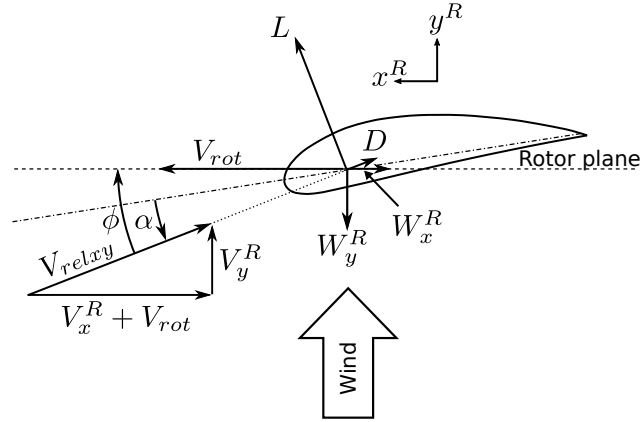
Figure 3. Cross-sectional airfoil element

while empirical results show higher values of C_T for induction factors above 0.3 - 0.5 (Eggleston and Stoddard, 1987). The current method uses a third order polynomial, as described by Madsen et al. (2018),

$$a = k_3 C_T^3 + k_2 C_T^2 + k_1 C_T \tag{5}$$

with coefficients $k_3 = 0.0883, k_2 = 0.0586, k_1 = 0.2460$ that fits to (4) for lower values of a and to empirical results and actuator disc simulations for higher loading (Madsen et al., 2010a).

For an annular ring element at radius r, the thrust coefficient is calculated by the formula presented by Madsen et al. (2018):

$$C_T = \frac{V_{relxy}^2 c C_y(\alpha) N_B}{2\pi r |\boldsymbol{V_0}|^2} \tag{6}$$

where V_{relxy} is the relative wind speed in the (x^R, y^R)-plane (see Fig. 3), c is the chord length, α is the angle of attack, N_B is the number of blades and C_y is the projection of the lift and drag coefficient into y^R:

$$C_y = cos(\phi) C_L(\alpha) + sin(\phi) C_D(\alpha) \tag{7}$$

where $\phi = \alpha + \theta_{twist} + \theta_{pitch}$ is the angle between V_{relxy} and the rotor plane.

From the measurements of a BMFS, V_{relxy} and α can be obtained directly, and the number of blades, the pitch angle, the radius, the chord length and the blade twist angle are assumed to be known. Hence, if the angle-of-attack dependent lift and drag coefficients are accessible from a look-up table, then the only unknown term on the right-hand side of (6) is $\boldsymbol{V_0}$. In aeroelastic simulations, $\boldsymbol{V_0}$ is obtained from the wind input model, but in this case, $\boldsymbol{V_0}$ is the wind speed that we want to find. It can, however, be found using the iterative approach described in section 3.4, such that the induced axial velocity can be calculated via equation 6, 5 and 3.

3.3.2 Tip correction

The relationship between the thrust coefficient and the axial induction factor stated in (4) is based on the assumption that the induced velocities are constant within an annular element. This is not the case for turbines with a finite number of blades and therefore Prandtl's tip loss factor, presented by Glauert (1935),

$$F_{tip} = \frac{2}{\pi} \cos^{-1} \left(\exp \left(-\frac{N_B}{2} \frac{R-r}{r\sin(\phi)} \right) \right) \tag{8}$$

where R is the blade tip radius, is applied in the current method by replacing C_T with $\frac{C_T}{F_{tip}}$ in (5) as described by Madsen et al. (2018). Calculating and applying the tip loss factor is straightforward as the only variable on the right-hand side, ϕ, can be calculated from the BMFS output.

3.3.3 Tangential induction

The tangential induction is a reaction to the torque force and results in a rotation of the wake downstream. The tangential velocity of the wake is defined in terms of the tangential induction factor, a':

$$W_x^R = a'\omega r \tag{9}$$

where ω is the angular velocity of the rotor. Unlike the axial induction, this effect does not affect the flow upstream. The amount of tangential induction at the position of a BMFS is therefore dependent on the sensor position relative to the blade, the pitch angle and the blade-deflection state. The current implementation of the method assumes full tangential induction, but for some applications, it may be more appropriate to switch it off.

The tangential induction factor is obtained by the formula presented by Madsen et al. (2018):

$$a' = \frac{V_{relxy}^2 c C_x(\alpha) N_B}{8\pi r^2 (1-a)|\boldsymbol{V_0}|\omega} \tag{10}$$

where $C_x = sin(\phi)C_L(\alpha) + cos(\phi)C_D(\alpha)$ is the projection of the lift and drag coefficient into x^R; see Fig. 3.

In (10), the only unknown term on the right-hand side is also $\boldsymbol{V_0}$, which can be found via the iterative approach described in section 3.4. To help this iterative procedure in finding the right solution, the value of a used in (10) is limited to the range $[0; 0.5]$.

3.3.4 Radial induction

The radial induction results in an expansion of the flow, as illustrated in Fig. 2. Introducing the radial induction factor, a_r, the radial induced velocity is:

$$W_z^R = |\boldsymbol{V_0}|a_r \tag{11}$$

The standard one-dimensional BEM theory does not handle radial induction and therefore the analytical equation derived by Madsen et al. (2010a) is used in the current method:

$$a_r = \frac{1}{2.24} \frac{C_{T,avg}}{4\pi} \ln\left(\frac{0.04^2 + \left(\frac{r}{R}+1\right)^2}{0.04^2 + \left(\frac{r}{R}-1\right)^2}\right) \tag{12}$$

where $C_{T,avg}$ is the average thrust coefficient of the whole rotor. In the current model, the revolution averaged local thrust
5 coefficient of the BMFS is used. This is obviously not the same, and the approximation is therefore only appropriate if the thrust coefficient of the radial position corresponds to the average thrust coefficient of the whole rotor. This is typically not the case near the root and the tip, and even for a sensor that is one third from the tip, some discrepancies must be expected.

3.3.5 Dynamic inflow

The induced velocities are parts of an equilibrium which is gradually established between the load on the blades, the rotor wake
10 and the induced velocity at the rotor plane (Sørensen and Aagaard Madsen, 2006).

   Small and high frequent turbulence is assumed to pass unaffected though the rotor and can therefore be measured directly, while the effect of large stationary turbulence eddies can be described by the BEM models in section 3.3.1 and section 3.3.3. In between, the modification of the wind flow depends on the wake recovery velocity. Snel and Schepers (1995) present different engineering approaches to model the wind turbine response in dynamic inflow.

15 In the current method, the model used in HAWC2 (Madsen et al., 2018) has been implemented with two modifications. This implementation applies two first-order low-pass filters to the induced velocities to model the slow and gradually changing induction,

$$\boldsymbol{W^R_{dyn}} = 0.6\mathrm{LP}(\tau_{NW}, \boldsymbol{W^R}) + 0.4\mathrm{LP}(\tau_{FW}, \boldsymbol{W^R}) \tag{13}$$

where $\mathrm{LP}(\tau, X)$ is a first-order low-pass filter. The two filters model the near- and far-wake effects respectively, and their filter
20 characteristics are given by:

$$\tau_{NW} = \tau_{NW}^* \frac{1.8R}{|\boldsymbol{V_0}| \min\left[1 - 3\frac{W^R_{y,avg}}{|\boldsymbol{V_0}|}, 2.0\right]} \tag{14}$$

$$\tau_{FW} = \tau_{FW}^* \frac{R}{|\boldsymbol{V_0}| \max\left[1 + 3\frac{W^R_{y,avg}}{|\boldsymbol{V_0}|}, 0.2\right]} \tag{15}$$

where

$$\tau_{NW}^* = -0.4783(r/R)^2 + 0.1025(r/R) + 0.6125 \tag{16}$$
25 $$\tau_{FW}^* = -0.4751(r/R)^2 + 0.4101(r/R) + 1.9210 \tag{17}$$

Equation (16) and (17) can be calculated straight away, while $\boldsymbol{V_0}$ and $W^R_{y,avg}$ are required for (14) and (15). $\boldsymbol{V_0}$ can be estimated as described in section 3.4, while the instant average axial induction of the whole rotor, $W^R_{y,avg}$, requires information from the

whole rotor which cannot be obtained from a BMFS.

In the current implementation, the revolution averaged local induction is used as an approximation. This means that the filter characteristics may be inaccurate if the induction at the radial position of the BMFS is not representative for the whole blade. The sensitivity to $W_{y,avg}^R$ is, however, limited and even extreme values have only a minor impact on the final estimated free

5   wind speed.

The other modification is more severe. In HAWC2, the rotor is discretised in grid points and the dynamic inflow model is applied to the local induced velocities of each of these grid points. This is possible because the local induction is calculated for each grid point in every time step, and this means that the induction of a certain grid point reflects the current circumstances as well as the history of that particular grid point.

10   In the current method, only the local induction at the position of the BMFS is obtainable as no information is available from other parts of the rotor. Applying the dynamic inflow model to the induced velocities at the position of the BMFS means that the estimated induction reflects the history of the moving BMFS instead of a fixed position. In a situation with wind shear, the estimated induction will therefore be too high in the lower part of the rotor and too low in the upper part, resulting in too much variation in the estimated free wind speed.

15   Instead, the low pass filters are applied to the induced wind speeds of fixed azimuthal positions. As the BMFS only passes a certain azimuthal position once per revolution, the sample frequencies of these signals are very low and some discrepancies must be expected.

Figure 4 shows the induced velocities in a simulation with turbulent inflow and shear. The quasi steady induced velocities estimated without the dynamic inflow model, W_y^R, are seen to vary much more than the HAWC2 reference, while applying

20   the low-pass filters to the rotating measurements, $W_{y,dyn}^R$, smoothens the induction too much. Applying the low-pass filters to the low-frequency signals of fixed azimuthal positions, $W_{y,dyn,azi}^R$, results in an estimate closer to the HAWC2 reference even though there is still some mismatch.

3.3.6   Skew inflow

In skewed inflow, where the mean wind is not perpendicular to the rotor plane, the axial induction is not directed exactly

25   towards the wind. Hence the speed of the inflow is reduced less, and the thrust is increased. Furthermore, variation in the wake vorticity concentration results in an azimuthal dependent variation of the axial induction; see Fig. 5.

The first effect is modelled by the method described in Madsen et al. (2018) where the axial induction factor is multiplied by a reduction factor, F_a, that is calculated from the average thrust coefficient, $C_{T,avg}$ and the skew inflow angle, Φ_r.

$$F_a = k_3 C_{T,avg}^3 + k_2 C_{T,avg}^2 + k_1 C_{T,avg} + k_0 \tag{18}$$
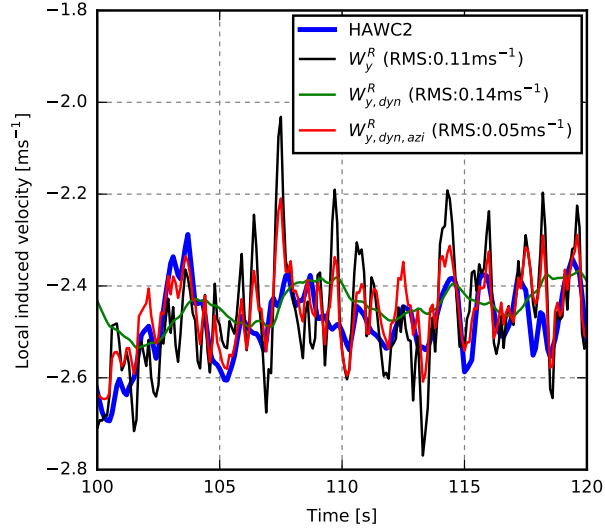
Figure 4. Local induced axial velocity calculated by HAWC2 and the current method in three configurations: W without the dynamic inflow model (W_y^R), with the dynamic inflow model applied to the rotating measurements ($W_{y,dyn}^R$), and with the dynamic inflow model applied to the low-frequency signals of fixed azimuthal positions ($W_{y,dyn,azi}^R$)
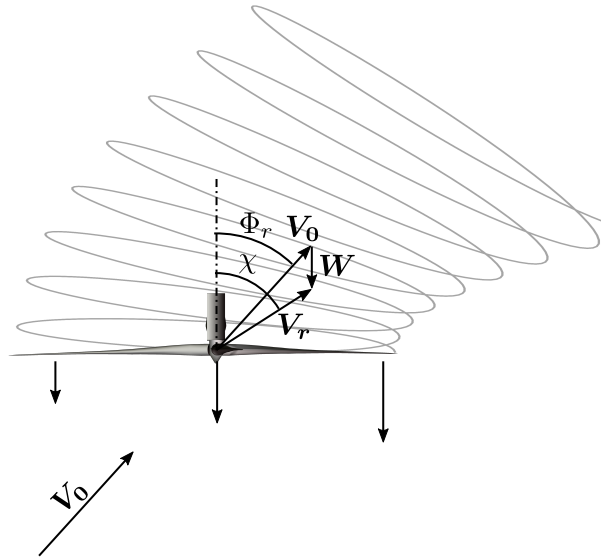
Figure 5. Wind turbine in skew inflow. The axial induction varies due to different wake vorticity concentration, and it is not directed exactly towards the wind

where

$$k_0 = 1 \tag{19}$$

$$k_1 = -0.164\Phi_r^3 + 0.4438\Phi_r^2 - 0.5136\Phi_r \tag{20}$$

$$k_2 = 0.8646\Phi_r^3 - 2.6145\Phi_r^2 + 2.1735\Phi_r \tag{21}$$

$$k_3 = -0.6481\Phi_r^3 + 2.1667\Phi_r^2 - 2.0705\Phi_r \tag{22}$$

The average thrust coefficient is estimated by the revolution averaged local thrust coefficient as described in section 3.3.4, and in this case the approximation is also expected to introduce discrepancies. The inflow angle, Φ_r, is calculated by

$$\Phi_r = \arctan\left(\frac{\sqrt{V_{0,x}^{R\,2} + V_{0,z}^{R\,2}}}{V_{0,y}^R}\right) \tag{23}$$

Note that the $C_{T,avg}$ used in (18) must be limited to the range $[0;1]$ as the model is invalid outside this range.

The azimuthal variation is calculated by a model presented by Madsen et al. (2018). In this model, the axial induction factor is multiplied with a rotor-position dependent factor, F_{azi}:

$$F_{azi} = 1 - k_x \frac{r}{R}\sin(\theta_{rotor}) - k_y \frac{r}{R}\cos(\theta_{rotor}) \tag{24}$$

where θ_{rotor} is the rotor-azimuth position. The factors, k_x and k_y, depend on the inflow angle, χ, in the horizontal and vertical plane (see Fig. 5):

$$k_x = \tan(0.4\chi_{hor}) \tag{25}$$

$$k_y = \tan(0.4\chi_{ver}) \tag{26}$$

3.3.7 Combining models

The presented aerodynamic models are now combined into a function, f_W, that comprises the following steps:

1. Calculate C_T using (6)

2. Calculate tip loss factor by (8)

3. Calculate a by (5) replacing C_T with $\frac{C_T}{F_{tip}}$

4. Apply skew inflow model

    (a) Calculate reduction factor F_a using (18)

    (b) Calculate azimuthal variation factor F_{azi} using (24)

    (c) Apply correction by multiplying a with F_a and F_{azi}

5. Calculate tangential induction factor using (10)

6. Calculate radial induction factor using (12)

7. Calculate the quasi-steady induced velocities $\boldsymbol{W^R} = \left(a'\omega r \quad a|\boldsymbol{V_0}| \quad |\boldsymbol{V_0}|a_r \right)^T$

8. Apply dynamic inflow model

    (a) Extract the induced velocities of each azimuthal position

    (b) calculate filter characteristics using (14) - (17)

    (c) Apply the dynamic inflow model (13) to the induced velocities of each azimuthal position to obtain $\boldsymbol{W^R_{dyn,azi}}$

Using this function, the estimated induced velocities can be calculated for a given $\boldsymbol{V_0}$,

$$\boldsymbol{W_{est}} = f_W(|\boldsymbol{V_0}|) \tag{27}$$

3.4 Estimating V_0

The flow velocity measured by the BMFS is the sum of the free flow and the induced velocities, hence:

$$\boldsymbol{V_0} = \boldsymbol{V_r} - \boldsymbol{W} \tag{28}$$

Using f_W, defined in section 3.3.7, an estimate of the free flow velocity can be obtained

$$\boldsymbol{V_{0,est}} = \boldsymbol{V_r} - f_W(|\boldsymbol{V_0}|) \tag{29}$$

Figure 6 shows the estimated free wind speed, $|\boldsymbol{V_{0,est}}|$, as a function of $|\boldsymbol{V_0}|$ in an example where the measured wind speed,
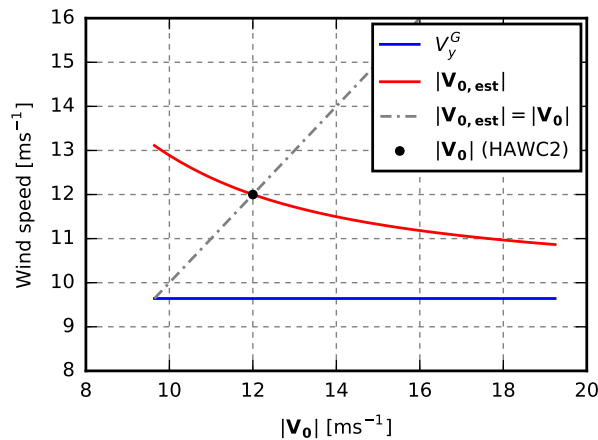
Figure 6. Example of free wind speed estimation. For $|V_0| = 12$, the estimated free wind speed, $|\boldsymbol{V_{0,est}}|$, calculated by (29) equals $|\boldsymbol{V_0}|$

$V_{r,y}^N$ is around $9.6 \, \mathrm{m \, s^{-1}}$.

We now want to find the correct free wind speed, i.e. the $\boldsymbol{V_0}$ that, when inserted into (29), results in $\boldsymbol{V_{0,est}}$ being equal to $\boldsymbol{V_0}$ ($12 \, \mathrm{m \, s^{-1}}$ in Figure 6). In other words, we solve

$$|\boldsymbol{V_0}| - |(\boldsymbol{V_r} - \mathrm{f_W}(\boldsymbol{V_0}))| = 0 \tag{30}$$

with respect to $\boldsymbol{V_0}$ iteratively using the Newton-Raphson method and $\boldsymbol{V_r}$ as the initial guess for $\boldsymbol{V_0}$.

3.5 Verification

3.5.1 HAWC2

The method is verified using HAWC2 simulations of a Siemens 3.6 MW turbine with a 107 m rotor. The turbine has a $6°$ tilt and $3.5°$ coning angle, and is controlled by the basic DTU Wind Energy controller (Hansen and Henriksen, 2013). The inflow turbulence for the turbulence cases is generated using the Mann model (Mann, 1994).

From the simulations, the relative wind speed is extracted at a point on the blade at radius 36 m, i.e. around one third from the tip. From this wind speed the estimated free wind speed is calculated and compared to the free wind speed used as the input to HAWC2. Note that the current version of HAWC2 (version 12.5) does not include radial induction, and therefore this model is disabled when testing against HAWC2.

As the current method is based on the same aerodynamic models as HAWC2, one may argue that this verification just adds and subtracts the same value, which obviously results in the original velocity. There are, however, differences that are important to investigate, e.g. the effect of the differences and approximation in the aerodynamic models of the current method, the effect of a flexible structure and the $\boldsymbol{V_0}$-estimation procedure.

3.5.2 EllipSys3D/Flex5

The method is furthermore verified using EllipSys3D/Flex5 simulations of a 2.3 MW Siemens turbine with a 93 m rotor. In these simulations, the flow field is obtained from large eddy simulations (LES) performed by the finite-volume and incompressible Navier-Stokes solver, EllipSys3D (Michelsen, 1992; Sørensen, 1995). The turbine is modelled using the actuator line method as developed by Sørensen and Shen (2002), where the individual blades are modelled by imposing body forces into the flow solver. The actuator lines are fully coupled to the aeroelastic tool, Flex5 (Øye, 1996), which models the structural dynamics according to the incoming flow; see (Sorensen et al., 2015) for details on the coupling. The inflow turbulence, which is similar to the turbulence of the HAWC2 simulations, is imposed 8.25 radius upstream from the rotor.

From these simulations, the flow speed is extracted at radius 32 m, i.e. also around one third from the tip. All EllipSys3D/Flex5 simulations use a flexible structural model. Flex5 is based on modal shape functions as opposed to the multibody formulation of HAWC2, and hence does not include torsional rotation of the blades.

To obtain the free inflow velocities, a separate identical flow simulation is performed, in which the effect of the aerodynamic forces on the flow is disabled such that the flow is not unaffected by the turbine. From this simulation the flow field in the vertical plane through the rotor centre is obtained for each time step.

3.5.3 Free flow reference

5 The estimated free flow velocities are based on the velocities measured at the sensor position (red dot in Fig. 7). In the current verification, however, the reference free flow velocity is extracted at the assumed (undeflected) sensor position (green dot in Fig. 7). This mismatch is expected to introduce some deviation as the turbulence is different at the two positions.

In the HAWC2 simulations, which are based on Taylor's frozen turbulence hypothesis, the turbulence is transported unaffected by the mean wind, i.e. with constant (free flow) speed along the y^G axis. This means that time can be mapped into space

10 and the free flow velocities can be extracted from the 3D turbulence field that is generated prior to the simulation.

The EllipSys flow, on the other hand, includes properties of real flow, e.g. that turbulence structures change and break up over time. The 3D turbulence field will therefore change in every time step and only the velocities at the rotor-centre flow plane are available for this study. The assumed sensor position, however, does not exactly intersect this plane, due to the rotor tilt angle. We are therefore compelled to rely on Taylor's frozen turbulence hypothesis to obtain the free flow reference velocity

15 at the assumed sensor position, but only from the rotor-centre plane to the sensor position (blue arrow in Fig. 7), i.e. at most 3.3 m.

Furthermore, the EllipSys flow is affected by the turbine. Near the rotor, the axial induction reduces the turbulence transport speed, while the radial induction results in an expansion of the flow that moves the turbulence structure outwards.

This means that the BMFS is exposed to "delayed" turbulence structures that originate from a smaller radial position (white

20 dot in Fig. 7), and even more deviation is therefore expected.
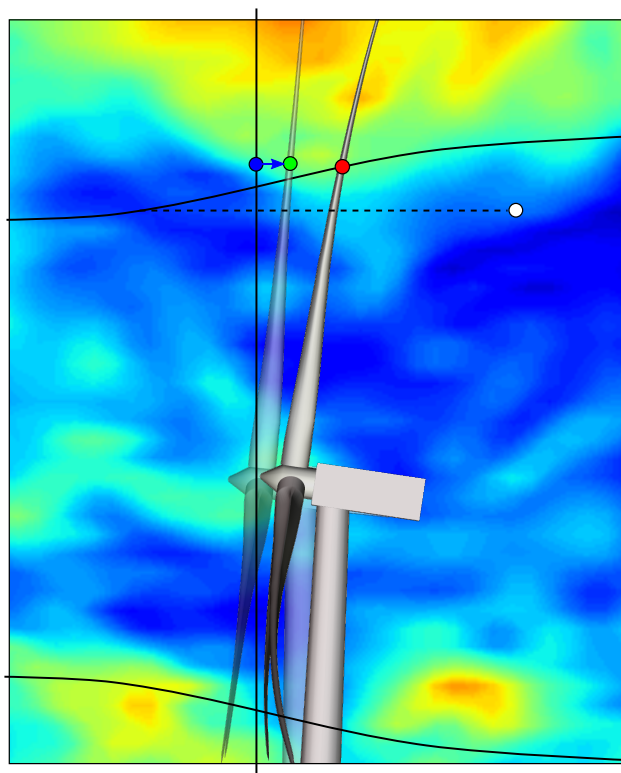
Figure 7. The estimated free flow at the sensor position (red dot) is compared to the free flow at the assumed position (green dot). In the EllipSys3D/Flex5 simulations, the nearest available free flow velocity is at the rotor-centre plane (blue dot). The sensor is, however, exposed to "delayed" turbulence structures that originate from a smaller radial position (white dot).

4   Results

4.1   HAWC2 verification

The root-mean-squared error, RMS, of the estimated instantaneous free wind speed, $\boldsymbol{V_{0,est}}$, is shown for $7\,\mathrm{m\,s^{-1}}$ in Fig. 8 for HAWC2 simulations of increasing complexity and the EllipSys3D/Flex5 simulations.
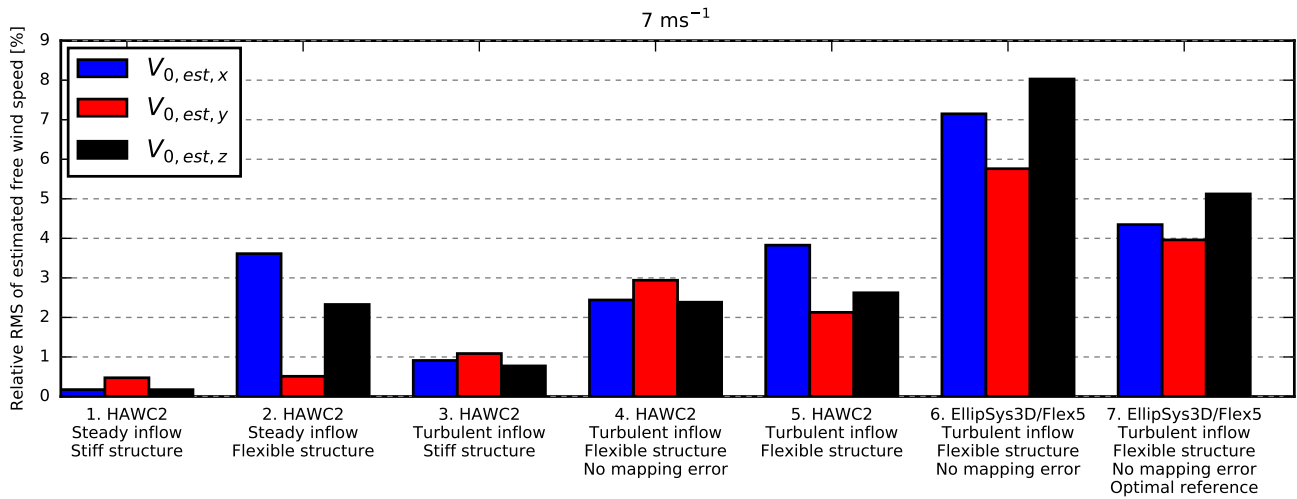
Figure 8. Relative RMS of the estimated free wind speed at $7\,\mathrm{m\,s^{-1}}$. For Case 4, 6 and 7, "No mapping error" means that deviations introduced in the transformation from the deflected blade-section coordinates to the fixed ground coordinates are not included

5   Starting with steady, uniform inflow and a stiff structural model, **Case 1**, the RMS error is very small and the minor deviations between the estimated free velocities and the HAWC2 references in Fig. 9 are caused by the effects of rotor tilt that are not exactly compensated by the skew inflow model.

In **Case 2**, the structural model is flexible. The rotation of the sensor due to the deflection and torsion of the tower and blade results in increased error levels that are clearly seen in the x- and z-velocity components in Fig. 9.

10   The most significant error is the $90°$ phase-shifted sinusoidal oscillation of the estimated velocities. This error is caused by thrust dependent flap-wise deflection of the blade that results in a part of $V_{r,y}^{R}$ being inaccurately projected onto the z^{R}-direction; see Fig. 10. This constant error leads to oscillations of the x and z components in the non-rotating ground coordinate system.

This error is reduced by a counteracting effect, namely the torque pushing the blade forward in the edge-wise direction.

15   At this forward-pushed position, the direction of the actual velocity due to rotor rotation, $\boldsymbol{V_{rot}}^{*}$, is slightly changed, but the blade-section coordinate system is rotated even more as seen in the right-hand side of Fig. 11. A small part of $\boldsymbol{V_{rot}}^{*}$ is thereby measured in the radial $-z^{R}$ direction, while the current model assumes the rotational velocity, $\boldsymbol{V_{rot}}$, to be tangential. This
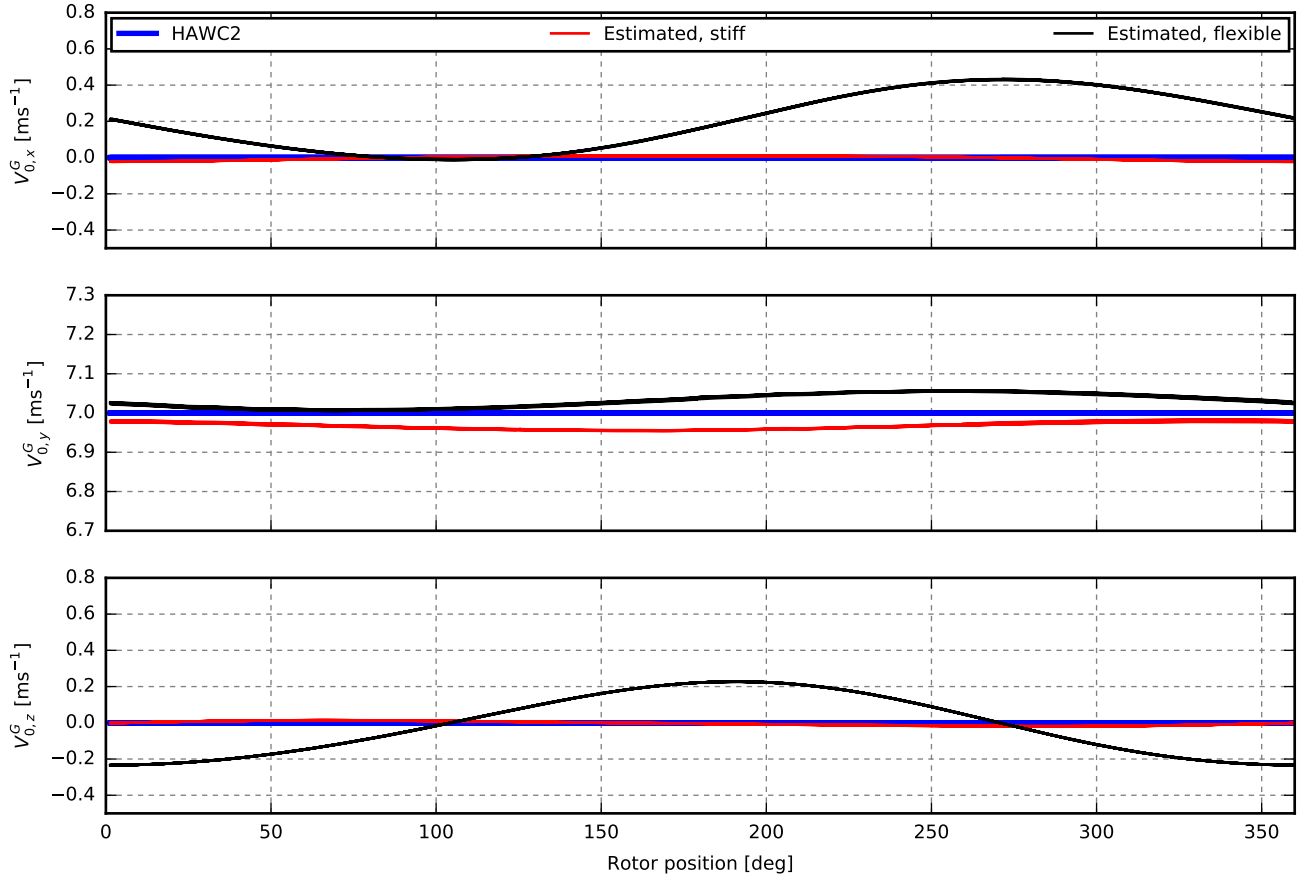
Figure 9. HAWC2 result: The free wind speed estimated in $13\,\mathrm{m\,s^{-1}}$ steady uniform inflow for stiff (Case 1) and flexible (Case 2) structural models.

mismatch leads to a torque-dependent error in the $-z^R$-direction that reduces the thrust-dependent contribution from flap-wise deflection.

A closer look at Fig. 9 reveals a positive offset in the estimated x-component. The reason for this offset, which corresponds to a spurious side wind, is a combination of two effects, both caused by gravity-induced edge-wise deflections of the blade. When the blades are horizontal, the gravity pulls the blades down towards the earth; see the left- and right-hand side of Fig. 11. This asymmetric edge-wise deflection leads to a small part of $\boldsymbol{V_{rot}}^*$ being measured in the radial $-z^R$ direction on the right-hand side of the rotor and in the $+z^R$-direction on the left-hand side, i.e. in the $+x^G$-direction on both sides. Furthermore, the transition from backward to forward deflection results in the blade moving faster in the upper part of the rotor and vice versa in the lower part. In the current method, however, the assumed rotational speed, $\boldsymbol{V_{rot}}$, is uniform. The mismatch results in deviations that also map to $+x^G$ in both vertical positions; see Fig. 11.

In combination, these two effects result in the almost constant positive offset of the $V_{0,est,x}^G$-velocity seen in Fig. 9.
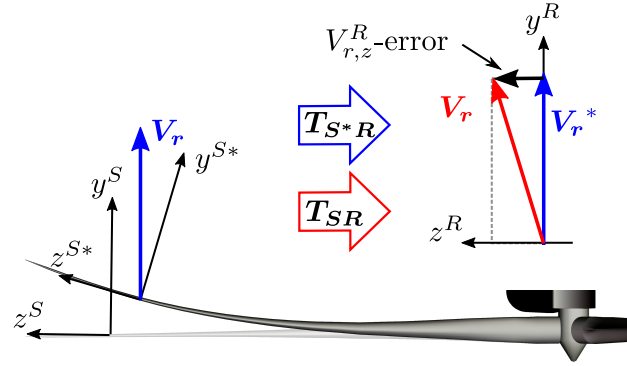
Figure 10. The rotation angle of the deflected blade section is unknown in the current method. An error is thereby introduced when mapping the measured wind speed, $\boldsymbol{V_r}$, from the blade section to the rotating rotor coordinates using the transformation matrix, $\boldsymbol{T_{SR}}$. The result is a constant error in the z^R-direction that leads to sinusoidal oscillations of the x- and z-component of the estimated free wind speed seen in Fig. 9
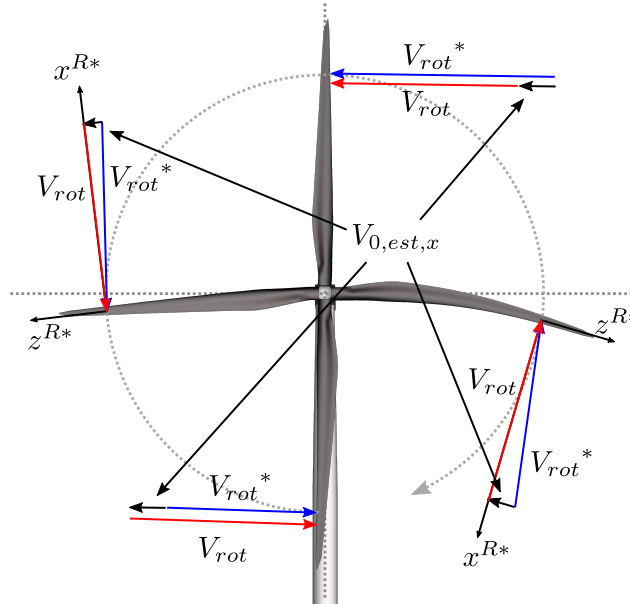
Figure 11. When the blades are horizontal, a small part of $\boldsymbol{V_{rot}}^*$ is measured in the $-z^{R*}$-direction on the right-hand side of the rotor and in the $+z^{R*}$-direction on the left-hand side due to the gravity induced deflection of the blade section. Furthermore, the blade is moving faster in the upper part of the rotor due to the transition from backward to forward deflection, and slower in the lower part. In the current method, however, the rotational speed, $\boldsymbol{V_{rot}}$, is assumed to be tangential and uniform. The mismatch results in a spurious side wind, seen as a mean offset in the x-component of Fig. 9.

For higher wind speeds, the estimated free wind speed in the y^G direction is overestimated due to the rotation of the elastic blade section. As the rotation angles are unknown in the current method, an error is introduced in the transformation from blade-section to ground coordinates; see Fig. 12. Blade torsion is an obvious source of the rotation, but for the current turbine model flap-wise bending also contributes considerably. This effect is highly dependent on the wind speed and blade design, and for the DTU 10MW reference wind turbine (Bak et al., 2013), an underestimation was seen instead.
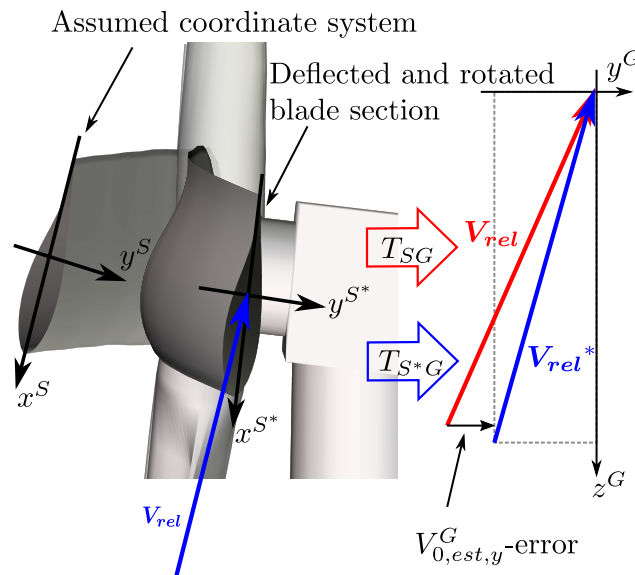
Figure 12. The torsion angle of the deflected blade section is unknown in the current method. An error is thereby introduced when mapping the relative velocity, $\boldsymbol{V_{rel}}$, from the blade section to the ground coordinates using the transformation matrix, $\boldsymbol{T_{SG}}$. The result is the overestimation of the y-component of the estimated free wind speed, $V_{0,est,y}^G$

Another effect that is seen in higher wind speeds is a negative mean offset in the z component due to tower deflection. In the transformation from rotating-rotor to ground coordinates, the angle between y^R and y^G is assumed to equal the tilt angle, but due to tower deflection the real angle is slightly larger, as it also includes the tower-top deflection angle, θ_{tt}; see Fig. 13. A small part of $\boldsymbol{V_r}$ is therefore inaccurately projected onto z^G, resulting in a small error in $V_{0,est,z}$.

This error can easily be compensated for by including the tower-top deflection angle, measured by an inclinometer, in the transformation from rotating rotor to ground coordinates. Similarly, the blade deflection and torsion angles can be included in the transformation from blade-section to rotor coordinates. These angles are, however, more challenging to measure, due to the large centrifugal force.

In **Case 3**, a stiff structural model is simulated in turbulent inflow. As seen in Fig. 8 and 14, the discrepancies are very limited despite the differences in the dynamic inflow model.

Case 4 combines the flexible structure with turbulent inflow, but the BMFS-measured flow velocities are extracted in the ground coordinates such that errors introduced in the transformation from deflected blade-section coordinates are avoided. The
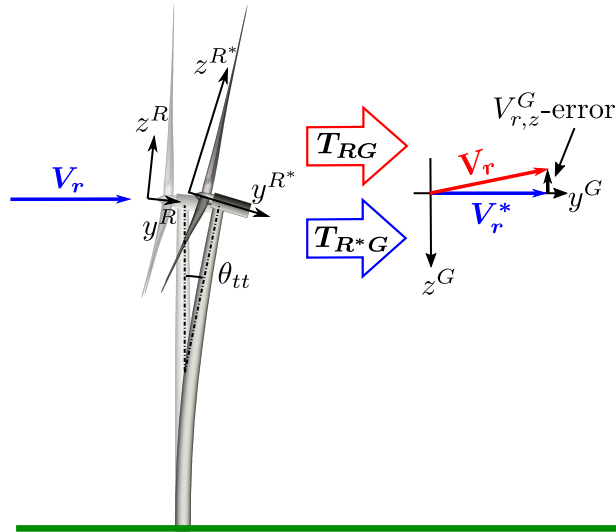
Figure 13. The tower top deflection angle, θ_{tt}, is unknown in the current method, and therefore the applied transformation matrix, $\boldsymbol{T_{RG}}$, inaccurately projects a small part of $\boldsymbol{V_r}$ onto $V_{r,z}^G$. The result is the small negative offset in the z-component in Fig. 9.

errors are significantly increased in all components; see Fig. 8. The reason is the mismatch between the assumed sensor velocity, i.e. the velocity due to rotor rotation and pitch motion, and the real velocity, which also includes velocity due to dynamic deflections of the structure. Furthermore, deviations are introduced because the free flow reference velocity is extracted at the assumed (undeflected) sensor position, while the model estimates the velocity at the deflected sensor position; see Fig. 7. This

5   mismatch can be reduced, assuming that the real sensor position can be measured, e.g. using a GPS, or estimated by a method that includes tower and blade deflection.
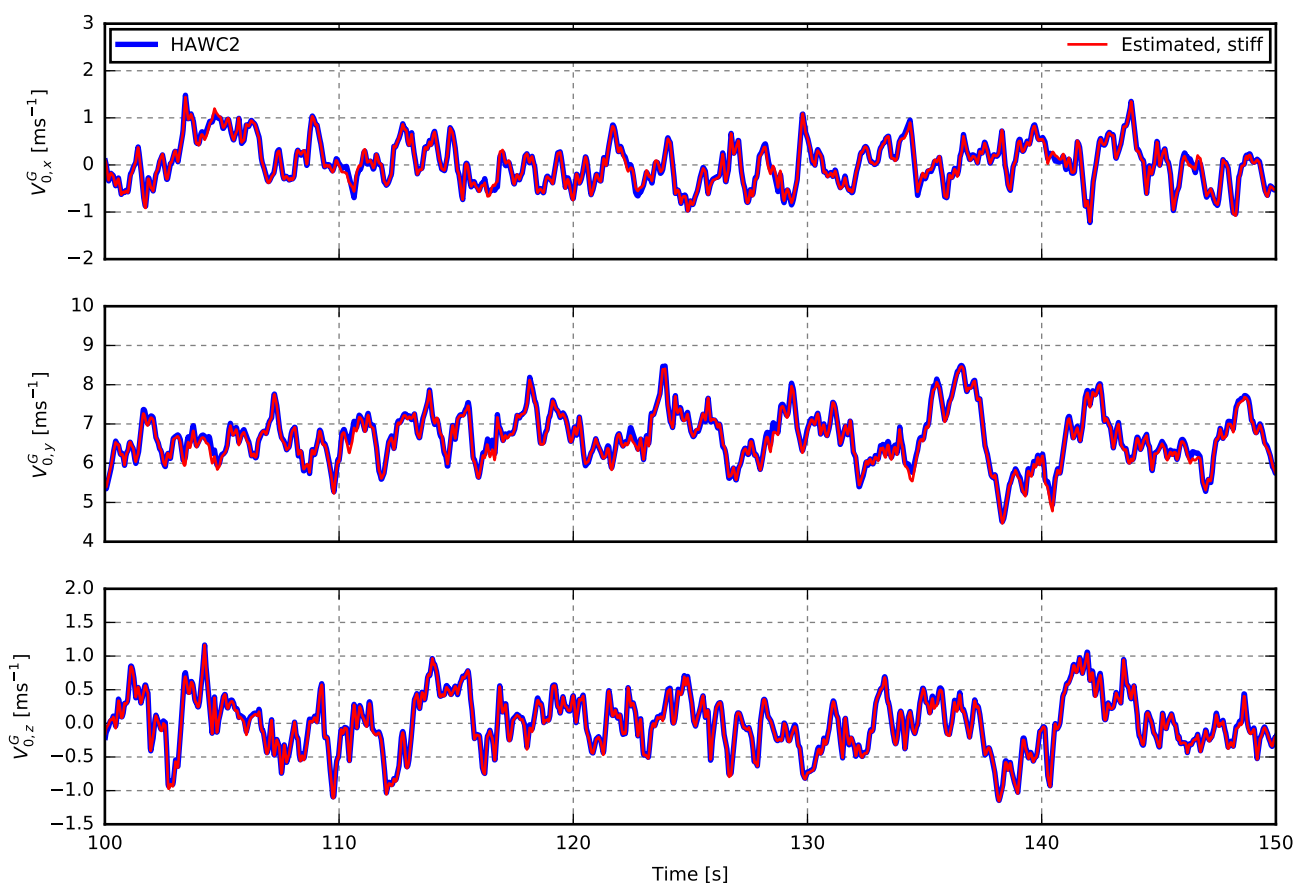
Figure 14. HAWC2 result: The free wind speed estimated in turbulent inflow for a stiff structural model (Case 3).

In **Case 5**, the BMFS-measured flow velocities are extracted in deflected blade-section coordinates and error is introduced due to the unknown orientation of this coordinate system; see Fig. 8 and 15. Higher RMS errors are therefore expected, but in this case, the error of the y component is reduced because the error due to coordinate transformation counteracts the error introduced by dynamic deflections.
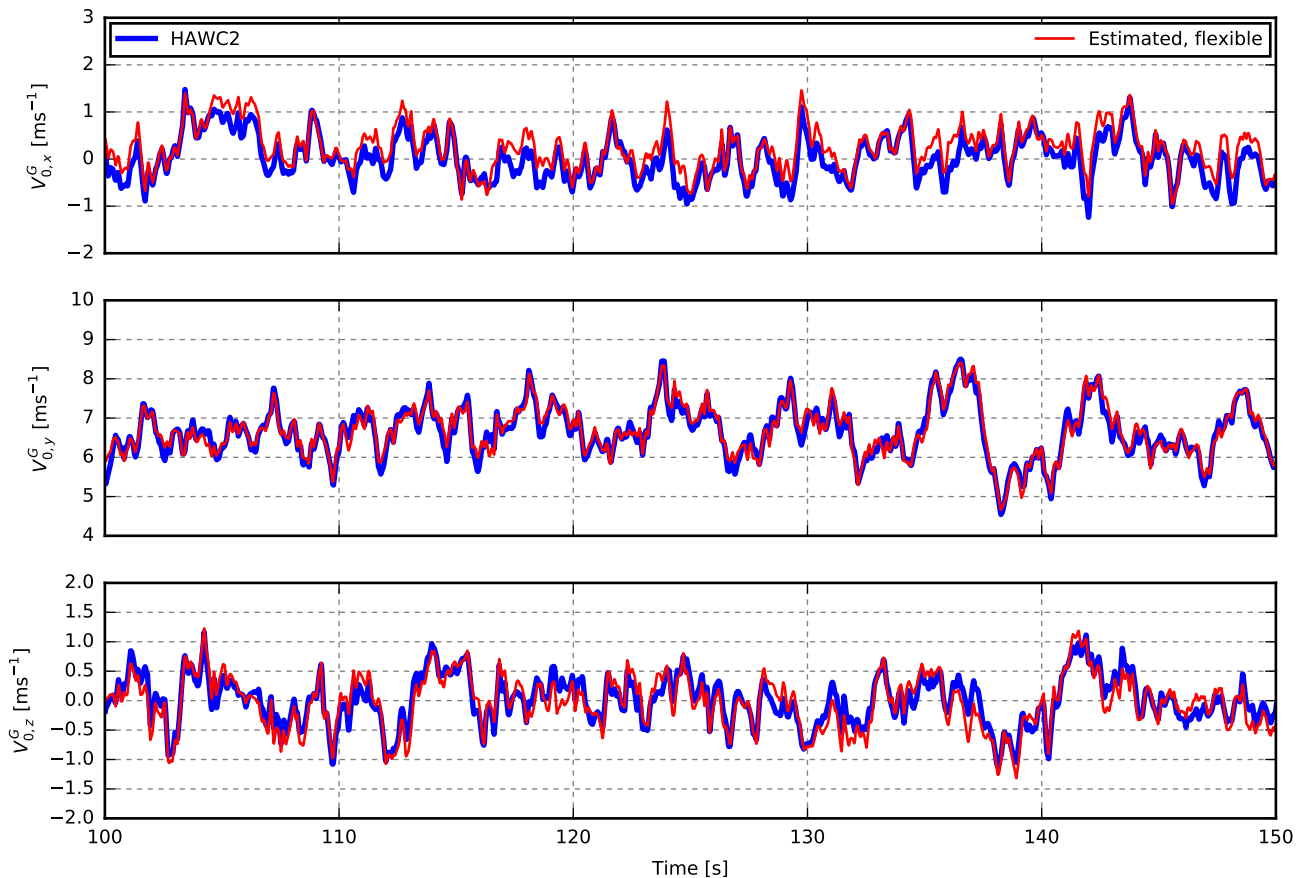
Figure 15. HAWC2 result: The free wind speed estimated in turbulent inflow for a flexible structural model (Case 5).

Figure 16 shows the power spectrum density of Case 5. The 1P (once per revolution) oscillating errors seen in the x and z component in Fig. 9 are seen around 0.2 Hz, while the deviations caused by dynamic deflections are seen in the y component above 0.4 Hz. At first it seems strange that the energy of the y component of the estimated free wind speed is lower than the HAWC2 reference, as the additional velocity due to the movement of the BMFS is expected to increase the energy. In reality, however, the deflection of the structure is correlated with the turbulence, as a blade exposed to a gust will deflect. This means that a BMFS that measures the gust relative to the deflecting blade will measure a less severe gust with less energy.
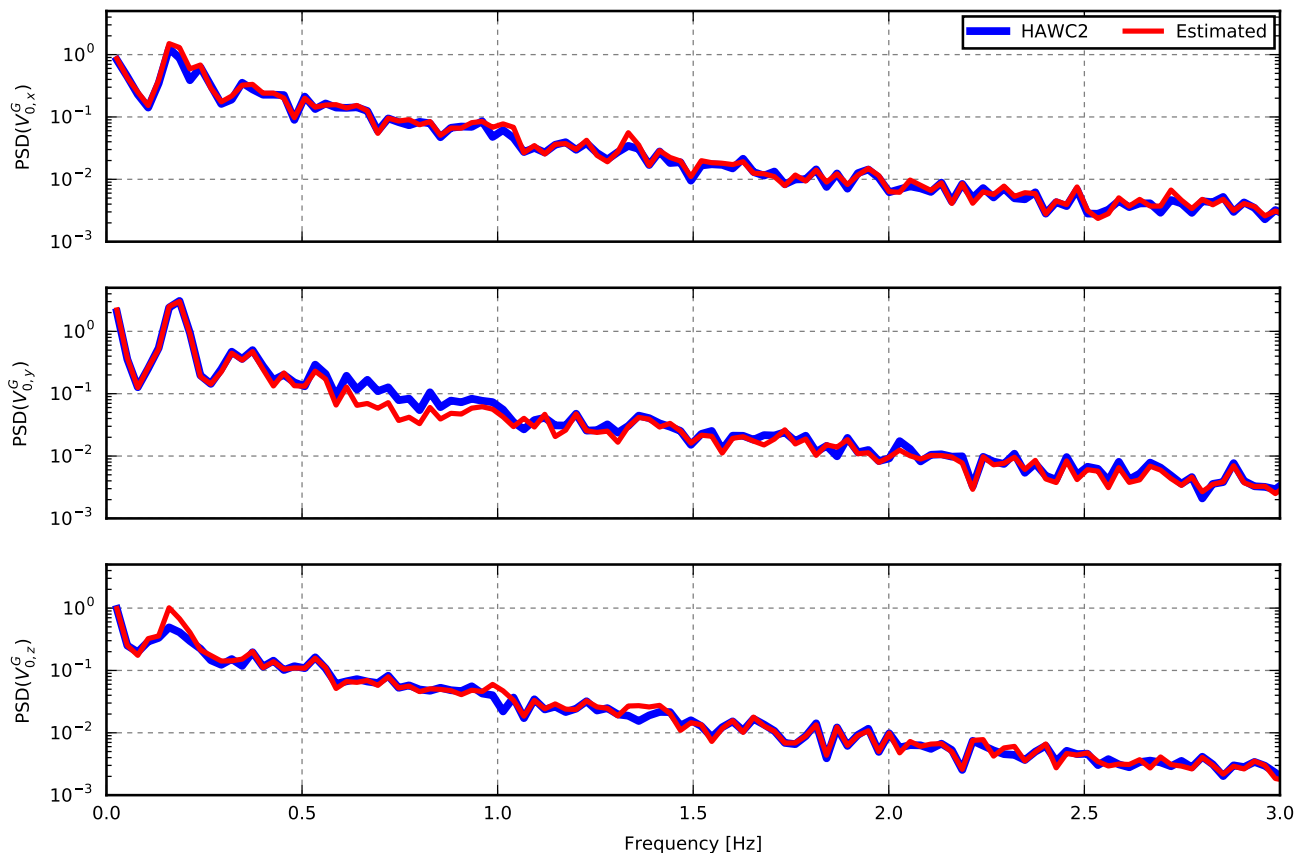
Figure 16. HAWC2 result:The power spectrum density of the free wind speed estimated in turbulent inflow for a flexible structural model.

Figure 17 shows the instant and revolution-averaged wind direction in a simulation with 20° yaw misalignment. The estimated wind direction is seen to follow the HAWC2 reference with a few degrees offset due to the spurious side wind caused by gravity induced edge-wise blade deflections.
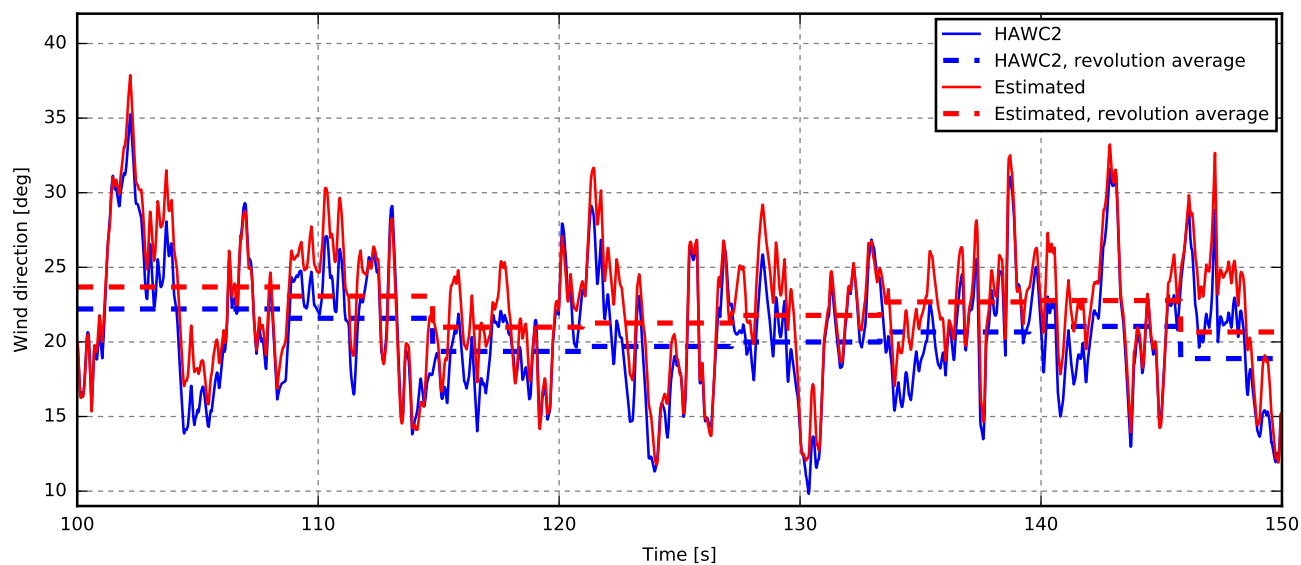
Figure 17. HAWC2 result: The wind direction derived from estimated free wind speed and HAWC2 reference in a simulation with $20°$ yaw misalignment.

Case 6 is based on the EllipSys3D/Flex5 simulations. The RMS errors are higher than in Case 4, which is the most equivalent HAWC2 case. Note, however, that the numbers are not directly comparable due to the different turbine sizes. The time series are compared in Fig. 18.
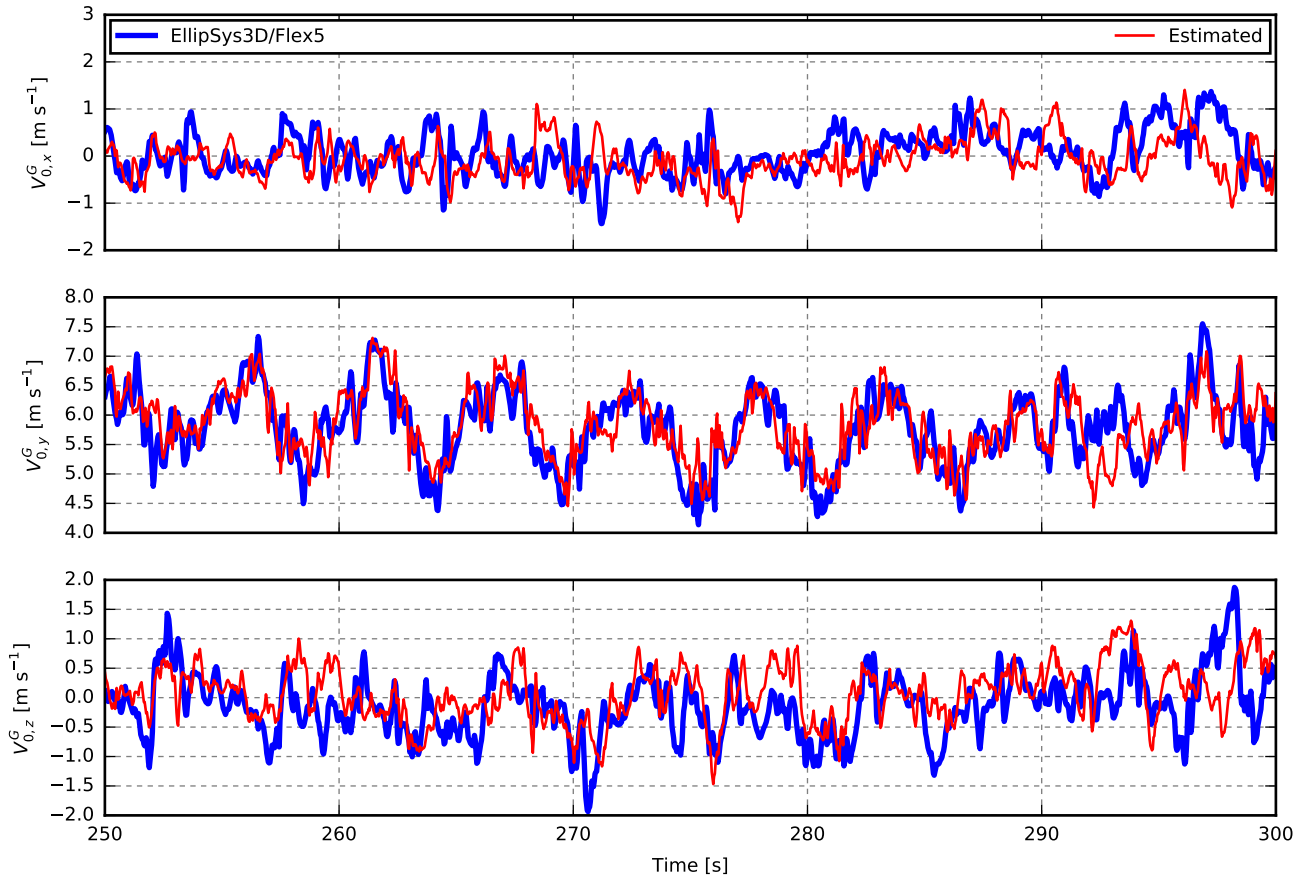
Figure 18. EllipSys3D/Flex5 result: The free wind speed estimated in turbulent inflow ($7\,\mathrm{m\,s^{-1}}$) based velocity in blade section coordinates (Case 6)

For the last case, **Case 7**, an optimisation routine was used to find the optimal reference position. For the $7\,\mathrm{m\,s^{-1}}$ the lowest RMS error was found when the estimated free velocities were compared to the free flow that hits the rotor-centre plane $2.2\,\mathrm{s}$ before and $4.2\,\mathrm{m}$ closer to the rotor centre. As seen in Fig. 8, the error is significantly reduced in all components. It is therefore concluded that the relatively high error of Case 6 is more related to the difference between the turbulence at the sensor and the reference position than to deviations introduced in the aerodynamic models and free flow estimation procedure.

Finally, Fig. 19 shows the difference between the free mean wind speed and estimated free mean wind speed at the position of the sensor, and similarly for the standard deviation. The HAWC2 results are based on 10 minutes of simulations of the Siemens 3.6 MW turbine. The deviations are mainly introduced in the mapping of velocities from the deflected blade-section

coordinate system to the ground coordinate system. The EllipSys3D/Flex5 results are based on 200 s of simulations of the Siemens 2.3 MW turbine. These velocities are extracted in ground coordinates; i.e. deviations due to mapping are not included. In Fig. 18, instantaneous deviations are seen, mainly because the turbulence at the sensor position is different from the free flow turbulence at the reference position due to expansion, delay and evolvement of the flow. In this case, however, most of these

5   deviations are averaged out, and the error in Fig. 19 is mainly introduced by differences in the induction modelling approach.

The error introduced in the transformation from deflected blade-section coordinates to ground coordinates are clearly seen in all components of the HAWC2 results. In the x component, the rotor speed and torque dependent spurious side wind increases the error of the mean wind speed up to rated rotor speed (around 9 $\mathrm{m\,s^{-1}}$). In the y component, the overestimation due to blade torsion is seen. The error in the mean wind speed in the z direction, due to tower deflection, increases with the thrust

10   up to rated wind speed (around 11 $\mathrm{m\,s^{-1}}$). Above rated wind speed, the error is rather constant as increased drag on the tower counterbalances the decrease in thrust. Finally, the error, due to flap-wise deflection of the blades, that results in the 1P oscillating deviations of the x and z components are clearly seen in the error of the standard deviation, which peaks with the thrust around rated wind speed.
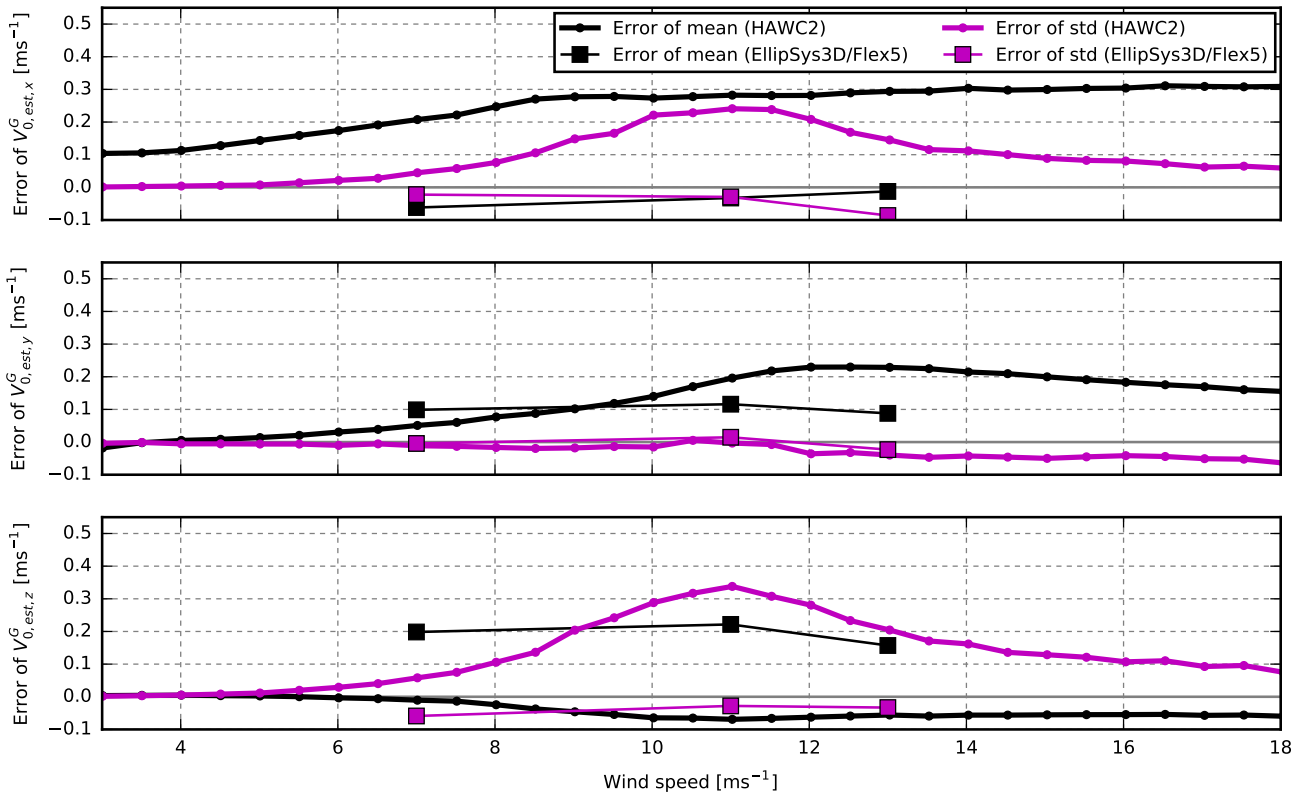
Figure 19. The difference between the mean/std of the free wind speed at the position of the sensor and the mean/std of the estimated free wind speed. The HAWC2 results are based on 10 minutes of simulations of the Siemens 3.6 MW turbine. The deviations are mainly introduced in the mapping of velocities from the deflected blade-section coordinate system to the ground coordinate system. The EllipSys3D/Flex5 results are based on 200 s of simulations of the Siemens 2.3 MW turbine. In this case, the deviations are mainly introduced by differences in the induction modelling approach. Both results are obtained from simulations of a flexible structure in turbulent inflow without shear.

5 Conclusions

In this paper, a method to estimate the undisturbed free inflow velocities from the flow velocities measured by a blade-mounted flow sensor, BMFS, has been presented and verified. The method includes a combination of aerodynamic models and procedures to estimate the free flow velocities from the measurements of a BMFS. The aerodynamic models comprise BEM-based

5   models for axial and tangential induction, a radial induction model and tip loss correction as well as models for skew and dynamic inflow. Some of these models require information, e.g. the average thrust coefficient of the whole rotor, that cannot be obtained from a BMFS. In these cases, approximations are used even though they are expected to introduce errors. Most of the models also take as input the free wind speed which is the final output of the current method. An iterative procedure is therefore used to find the estimated free wind speed.

10   The method has been verified on HAWC2 simulations. This verification reveals that the method works well and provides accurate results when using a stiff structural model. Using a flexible structural model, larger deviations are seen. These deviations are caused by the rotation of the sensor due to the deflection and torsion of the tower and blade, movement of the sensor due to turbulence induced dynamic deflections of the structure, and the mismatch between the turbulence at the real deflected sensor position and the reference position, i.e. the assumed (undeflected) sensor position. These effects are highly dependent

15   on the wind speed and the structural design.

Furthermore, the method has been verified by simulations performed using EllipSys3D/Flex5; a flexible structural model coupled with a large eddy simulation (LES) flow solver. In these results, the free velocities estimated by the current method deviate more from the simulated free velocities, but it is concluded that the error is more related to the difference between the turbulence at the sensor and the reference position than to errors introduced in the aerodynamic models and free flow estimation

20   procedure.

Data availability. Simulation results are not available due to confidentiality.

Competing interests. The authors declare that they have no conflict of interest.

Acknowledgements. The authors would like to acknowledge Siemens Wind Power for providing data for the simulation model.

References

Bak, C., Zahle, F., Bitsche, R., Kim, T., Yde, A., Henriksen, L. C., Hansen, M. H., Blasques, J. P. A. A., Gaunaa, M., and Natarajan, A.: The DTU 10-MW Reference Wind Turbine, Tech. rep., Presented at Danish Wind Power Research 2013, Fredericia, Denmark, 27/05/2013, www.orbit.dtu.dk, 2013.

5 Barlas, T., van der Veen, G., and van Kuik, G.: Model predictive control for wind turbines with distributed active flaps: incorporating inflow signals and actuator constraints, Wind Energy, 15, 757–771, https://doi.org/10.1002/we.503, http://doi.wiley.com/10.1002/we.503, 2012.

Brand, A., Dekker, J., de Groot, C., and Späth, M.: Overview of aerodynamic measurements on an Aerpac 25 WPX wind turbine blade at the HAT 25 experimental wind turbie, ECN-DE-Memo-96-014, ECN, 1996.

Eggleston, D. M. and Stoddard, F. S.: Wind turbine engineering design, Van Nostrand Reinhold,, 1987.

10 Elliott, D. L. and Cadogan, J. B.: Effects of wind shear and turbulence on wind turbine power curves, in: Wind Energy, pp. 10–14, Pacific Northwest Lab., Richland, WA (USA), Presented at the European Community Wind Energy Conference and Exhibition, Madrid, Spain, 10-14 Sep. 1990, http://www.osti.gov/scitech/servlets/purl/6348447, 1990.

Glauert, H.: Airplane Propellers, pp. 169–360, Springer Berlin Heidelberg, Berlin, Heidelberg, https://doi.org/10.1007/978-3-642-91487-4_3, 1935.

15 Guntur, S. and Sørensen, N. N.: An evaluation of several methods of determining the local angle of attack on wind turbine blades, Journal of Physics: Conference Series, 555, 12 045, http://stacks.iop.org/1742-6596/555/i=1/a=012045, 2014.

Hansen, M. H. and Henriksen, L. C.: Basic DTU Wind Energy controller, Tech. rep., DTU Wind Energy, www.orbit.dtu.dk, 2013.

Kragh, K. and Hansen, M.: Individual Pitch Control Based on Local and Upstream Inflow Measurements, in: 50th AIAA Aerospace Sciences Meeting including the New Horizons Forum and Aerospace Exposition, Reston, Virigina, Aerospace Sciences Meetings, American
20 Institute of Aeronautics and Astronautics, https://doi.org/10.2514/6.2012-1021, 2012.

Kragh, K. A., Henriksen, L. C., and Hansen, M. H.: On the Potential of Pitch Control for Increased Power Capture and Load Alleviation, in: Torque, the science of making torque from wind., Presented at The Science of Making Torque from Wind 2012, 9–11 October 2012, Oldenburg, Germany, www.orbit.dtu.dk, 2012.

Larsen, T. J. and Hansen, A. M.: How 2 HAWC2, the user's manual, no. December in Denmark. Forskningscenter Risoe. Risoe-R, Technical
25 Report, Risø National Laboratory, Roskilde, Denmark, www.orbit.dtu.dk, 2007.

Larsen, T. J., Aagaard Madsen, H., and Thomsen, K.: Active load reduction using individual pitch, based on local blade flow measurements, Wind Energy, 8, 67–80, https://doi.org/10.1002/we.141, 2005.

Larsen, T. J., Aagaard Madsen, H., Larsen, G. C., and Hansen, K. S.: Validation of the dynamic wake meander model for loads and power production in the Egmond aan Zee wind farm, Wind Energy, 16, 605–624, https://doi.org/10.1002/we.1563, 2013.

30 Madsen, H. A.: Risø-M-2902: Aerodynamics and Structural Dynamics of a Horizontal Axis WindTurbine - Raw Data Overview, Technical Report Risø-M-2902, Risø National Laboratory, Roskilde, Denmark, 1991.

Madsen, H. A.: Correlation of amplitude modulation to inflow characteristics, Proceedings of 43rd International Congress on Noise Control Engineering, http://www.acoustics.asn.au/conference{_}proceedings/INTERNOISE2014/papers/p171.pdf, 2014.

Madsen, H. A., Thomsen, K., and Petersen, S. M.: Risø-I-210: Wind Turbine Wake Data from Inflow Measurements using a Five hole Pitot
35 Tube on a NM80 Wind Turbine Rotor in the Tjæreborg Wind Farm, Tech. Rep. December, be, 2003.

Madsen, H. A., Bak, C., Døssing, M., Mikkelsen, R. F., and Øye, S.: Validation and modification of the Blade Element Momentum theory based on comparisons with actuator disc simulations, Wind Energy, 13, 373–389, https://doi.org/10.1002/we.359, 2010a.

Madsen, H. A., Bak, C., Schmidt Paulsen, U., Gaunaa, M., Fuglsang, P., Romblad, J., Olesen, N. A., Enevoldsen, P., Laursen, J., and Jensen, L.: The DAN-AERO MW Experiments: Final report, Denmark. Forskningscenter Risoe. Risoe-R, Danmarks Tekniske Universitet, Risø Nationallaboratoriet for Bæredygtig Energi, www.orbit.dtu.dk, 2010b.

Madsen, H. A., Larsen, T. J., Pirrung, G., Verelst, D., and Zahle, F.: An implementation of the BEM model for simulation of non-uniform loading and inflow, To be published, 2018.

Mann, J.: The spatial structure of neutral atmospheric surface-layer turbulence, Journal of Fluid Mechanics, 273, 141, https://doi.org/10.1017/S0022112094001886, 1994.

Medina, P., Singh, M., Johansen, J., Jove, A. R., Machefaux, E., Fingersh, L. J., and Schreck, S.: Aerodynamic and performance measurements on a SWT-2.3-101 wind turbine, Tech. rep., National Renewable Energy Laboratory (NREL), Golden, CO., 2011.

Meyer Forsting, A. R., Troldborg, N., Murcia Leon, J. P., Sathe, A., Angelou, N., and Vignaroli, A.: Validation of a CFD model with a synchronized triple-lidar system in the wind turbine induction zone, Wind Energy, 20, 1481–1498, https://doi.org/10.1002/we.2103, 2017.

Michelsen, J. A.: Basis3D – a Platform for Development of Multiblock PDE Solvers, Tech. rep., Danmarks Tekniske Universitet, 1992.

Mikkelsen, T., Mann, J., Courtney, M., Sjöholm, M. M., Mann, J., Courtney, M., and M: Windscanner: 3-D wind and turbulence measurements from three steerable doppler lidars, IOP Conference Series: Earth and Environmental Science, 1, 12 018, http://stacks.iop.org/1755-1315/1/i=1/a=012018, 2008.

Mikkelsen, T., Hansen, K. H., Angelou, N., Sjöholm, M., Harris, M., Hadley, P., Scullion, R., Ellis, G., and Vives, G.: Lidar wind speed measurements from a rotating spinner, in: European Wind Energy Conference and Exhibition, www.orbit.dtu.dk, 2010.

Øye, S.: FLEX4 simulation of wind turbine dynamics, in: Proceedings of 28th IEA Meeting of Experts Concerning State of the Art of Aeroelastic Codes for Wind Turbine Calculations. Available through International Energy Agency., pp. 71–76, Danmarks Tekniske Universitet, Lyngby, Denmark, 1996.

Pedersen, M. M., Larsen, T. J., Larsen, G. C., Madsen, H. A., and Toldborg, N.: Turbulent wind field characterization and re-generation based on pitot tube measurements mounted on a wind turbine, in: 33rd Wind Energy Symposium, AIAA SciTech, American Institute of Aeronautics and Astronautics, Kissimmee, Florida, https://doi.org/10.2514/6.2015-1467, 2015.

Pedersen, M. M., Larsen, T. J., Madsen, H. A., and Larsen, G. C.: Using wind speed from a blade-mounted flow sensor for power and load assessment on modern wind turbines, Wind Energy Science, 2, 547–567, https://doi.org/10.5194/wes-2-547-2017, 2017.

Petersen, J. T. and Aagaard Madsen, H.: Risø-R-993(EN): Local Inflow and Dynamics – Measured and Simulated on a Rotating Wind Turbine Blade, Risø National Laboratory, Roskilde, Denmark, 1997.

Rahimi, H., Schepers, G., Shen, W. Z., García, N. R., Schneider, M., Micallef, D., Ferreira, C. S., Jost, E., Klein, L., and Herráez, I.: Evaluation of different methods for determining the angle of attack on wind turbine blades with CFD results under axial inflow conditions, arXiv preprint arXiv:1709.04298, 2017.

Schepers, J. G., Brand, A. J., Bruining, A., Hand, M., Infield, D., Madsen, H., Maeda, T., Paynter, J., van Rooij, R., and Shimizu, Y.: Final report of IEA Annex XVIII: enhanced field rotor aerodynamics database, Energy Research Center of the Netherlands, ECN-C-02-016, February, ftp://ftp.ecn.nl/pub/www/library/report/2002/c02016.pdf, 2002.

Scholbrock, A. K., Fleming, P. A., Wright, A., Slinger, C., Medley, J., and Harris, M.: Field Test Results from Lidar Measured Yaw Control for Improved Power Capture with the NREL Controls Advanced Research Turbine, in: 33rd Wind Energy Symposium, AIAA SciTech Forum, American Institute of Aeronautics and Astronautics, Reston, Virginia, https://doi.org/10.2514/6.2015-1209, 2015.

Shen, W. Z., Hansen, M. O. L., and Sørensen, J. N.: Determination of Angle of Attack (AOA) for Rotating Blades, www.orbit.dtu.dk, 2006.

Shen, W. Z., Hansen, M. O. L., and Sørensen, J. N.: Determination of the angle of attack on rotor blades, Wind Energy, 12, 91–98, https://doi.org/10.1002/we.277, 2009.

Simms, D. A., Hand, M. M., Fingersh, L. J., and Jager, D. W.: Unsteady aerodynamics experiment phases II-IV test configurations and available data campaigns, Tech. rep., National Renewable Energy Lab, https://www.nrel.gov/docs/fy99osti/25950.pdf, 1999.

5 Snel, H. and Schepers, J. G.: Joint investigation of dynamic inflow effects and implementation of an engineering method, Netherlands Energy Research Foundation ECN, https://www.ecn.nl/publications/E/1995/ECN-C--94-107, 1995.

Sørensen, J. N. and Shen, W. Z.: Numerical modelling of Wind Turbine Wakes, J. Fluids Eng., 124, 393–399, https://doi.org/10.1115/1.1471361, 2002.

Sorensen, J. N., Mikkelsen, R. F., Henningson, D. S., Ivanell, S., Sarmast, S., and Andersen, S. J.: Simulation of wind turbine wakes using

10 the actuator line technique, Philosophical Transactions of the Royal Society A: Mathematical, Physical and Engineering Sciences, 373, 20140071–20140071, https://doi.org/10.1098/rsta.2014.0071, 2015.

Sørensen, N. N.: General Purpose Flow Solver Applied to Flow over Hills, Ph.D. thesis, Technical University of Denmark, www.orbit.dtu.dk, 1995.

Sørensen, N. N. and Aagaard Madsen, H.: Modelling of transient wind turbine loads during pitch motion, in: paper and poster). In: Proceed-

15 ings (online). 2006 European Wind Energy Conference and Exhibition, Athens (GR), vol. 27, 2006.

St. Martin, C. M., Lundquist, J. K., Clifton, A., Poulos, G. S., and Schreck, S. J.: Wind turbine power production and annual energy production depend on atmospheric stability and turbulence, Wind Energ. Sci., 1, 221–236, https://doi.org/10.5194/wes-1-221-2016, 2016.

Taylor, G. I.: The Spectrum of Turbulence, Proceedings of the Royal Society A: Mathematical, Physical and Engineering Sciences, 164, 476–490, https://doi.org/10.1098/rspa.1938.0032, 1938.

20 Troldborg, N. and Meyer Forsting, A. R.: A simple model of the wind turbine induction zone derived from numerical simulations, Wind Energy, https://doi.org/10.1002/we.2137, http://doi.wiley.com/10.1002/we.2137, 2017.

Wagner, R., Vignaroli, A., Angelou, N., Sathe, A., Meyer Forsting, A. R., Sjöholm, M., and Mikkelsen, T. K.: Measurement of turbine inflow with a 3D windscanner system and a spinnerlidar, www.orbit.dtu.dk, 2015.